PAPER

Check for updates

The efficient removal of Sr²⁺ using two thiostannates *via* ion exchange

Yu-Wei Ren,[a,b,c] Jia-Hua Luo,[a,b,c] Zhi-Hua Chen,[b,c] Shu-Zhen Liu,[a,b,c] Xin-Ping Guo,[a,b,c] Guo-Yang Chen,[a,b,c] Mei-Ling Feng [b,c] * and Xiao-Ying Huang [b,c]

^{90}Sr is one of the most hazardous radionuclides in spent fuel, as it releases high energy β radiation accompanied by the release of a large amount of heat. Its easy environmental mobility and calcium-like bioconcentration properties pose a serious threat to the ecological environment and human health. Therefore, the efficient removal of ^{90}Sr from complex aqueous environments is of great significance. Herein, two new isomorphic thiostannates $K_2Sn_2S_5 \cdot H_2O$ and $K_{1.1}Rb_{0.9}Sn_2S_5 \cdot H_2O$, namely FJSM-KSnS and FJSM-KRbSnS, respectively, were prepared by the solvothermal method. Their structures feature a two-dimensional (2D) wavy anionic layer of $[Sn_2S_5]_n^{2n-}$ with big windows of ten-membered rings. Alkali metal cations (K⁺/Rb⁺) as charge balancers as well as H_2O molecules are located in the interlayer spaces. They exhibit efficient Sr²⁺ removal performance with high adsorption capacities (q_m^{Sr} = 59.88 mg g⁻¹ for FJSM-KSnS, q_m^{Sr} = 62.82 mg g⁻¹ for FJSM-KRbSnS). FJSM-KSnS as a representative exhibits fast kinetics (equilibrium within 10 minutes) and good selectivity for Sr²⁺ removal in the presence of excessive Na⁺, and even in actual environmental water samples. In addition, the Sr²⁺ capture mechanism is revealed by energy-dispersive X-ray spectroscopy, elemental distribution mapping, and X-ray photoelectron spectroscopy characterization. The efficient capture of Sr²⁺ is attributed to the ion exchange between Sr²⁺ and interlayered alkali metal ions of thiostannates. This work expands the structural types of thiostannates and provides new efficient ion exchange materials for radiostrontium remediation.

Introduction

^{90}Sr (a half-life of 28.6 years) emitting β radiation (maximum energy of 0.546 MeV) is one of the most hazardous radionuclides produced by the nuclear fission process.[1,2] It is highly water-soluble (usually in the form of ^{90}Sr²⁺ ions in nuclear waste liquids) and environmentally mobile, which significantly increases the risk of ecological hazards if it diffuses in water systems.[3] In addition, due to its chemical similarity to calcium, it is easily absorbed by organisms through the food chain and preferentially accumulates in bones and teeth, posing a threat to human health.[4,5] On the other hand, ^{90}Sr can be used as a β radiation source in a variety of medical and industrial applications, such as radiation therapy, densitometry, and radioisotope thermoelectric generators.[6–8] Therefore, the efficient capture of ^{90}Sr from complex radioactive liquid

wastes is of vital significance for ecological protection, human health, and resource utilization. However, the strong water solubility and high mobility of ^{90}Sr, as well as the complex composition of radioactive waste liquids, pose a great challenge for its efficient capture.[9]

Currently, mainstream techniques for capturing Sr²⁺ include chemical precipitation,[10,11] solvent extraction,[12–14] and adsorption/ion exchange.[15–17] However, the chemical precipitation method generally suffers from low adsorption capacity and poor selectivity.[18] Although the solvent extraction method can improve the separation efficiency, it faces the problems of high cost limitations and secondary waste liquid.[19] By contrast, the ion exchange method is regarded as a more desirable solution for Sr²⁺ capture due to its ease of operation, efficient treatment capacity, and low secondary waste generation.[20–22] To date, a variety of ion exchange materials have been developed for Sr²⁺ removal, including zeolites,[23] clays,[24] titanates,[25] silica-based materials,[26] and so on. Nevertheless, these reported materials still have limitations such as slow dynamics, low adsorption capacity, and insufficient selectivity.[27]

Metal sulfide ion exchangers (MSIEs) are a class of highly promising ion exchange materials developed in recent years,

*ªCollege of Chemistry, Fuzhou University, Fuzhou 350116, Fujian, China.
E-mail: fml@fjirsm.ac.cn*
ᵇState Key Laboratory of Structural Chemistry, Fujian Institute of Research on the Structure of Matter, Chinese Academy of Sciences, Fuzhou, Fujian 350002, China
ᶜFujian College, University of Chinese Academy of Sciences, Fuzhou 350002, P.R. China

where cations residing in the interlayer spaces or channels to balance the charge of thiometallate can be exchanged by radio-nuclide ions (such as $^{90}Sr^{2+}$, $^{137}Cs^+$, and UO_2^{2+}) in the water body to achieve the removal of radionuclides.[28–32] Notably, the anionic framework of MSIEs contains Lewis soft base S^{2-}, exhibiting strong affinity for relatively soft Lewis acidic metal ions.[33] The high polarizability of the soft base S^{2-} promotes the deformation of the metal sulfide bonds (M–S), resulting in a relatively flexible metal sulfide framework that can usually exhibit "breathing action" to effectively trap and anchor the target ions in the structure.[34] Therefore, the softly basic and flexible framework of MSIEs facilitates the efficient removal of target radioactive ions. Most of the reported MSIEs including $K_{2x}Mn_xSn_{3-x}S_6$ (x = 0.5–0.95, KMS-1),[35] $K_{2x}Mg_xSn_{3-x}S_6$ (x = 0.5–1, KMS-2),[36] and $K_{2x}Sn_{4-x}S_{8-x}$ (x = 0.65–1, KTS-3)[37] exhibit excellent capture ability for Cs^+. KMS-1 and KTS-3 can quickly capture Cs^+ within 5 minutes,[35,37] and the adsorption capacity (q_m^{Sr}) of KMS-2 for Cs^+ reaches astonishing 531 mg g^{-1}.[36] However, even if some MSIEs can trap both Cs^+ and Sr^{2+}, their Sr^{2+} capture performance is not outstanding, usually suffering from the disadvantages of low adsorption capacity and slow kinetics.[36,38–43] For example, the maximum Sr^{2+} adsorption capacity of $K_{1.87}ZnSn_{1.68}S_{5.30}$ (KZTS) is only 19.3 mg g^{-1},[40] and $Na_5Zn_{3.5}Sn_{3.5}S_{13}·6H_2O$ (ZnSn-1) requires 1440 min to reach saturation adsorption of Sr^{2+}.[41] Therefore, it is urgent to develop new MSIEs that can efficiently capture Sr^{2+}.

Herein, two new two-dimensional (2D) layered thiostannates, namely $K_2Sn_2S_5·H_2O$ (FJSM-KSnS) and $K_{1.1}Rb_{0.9}Sn_2S_5·H_2O$ (FJSM-KRbSnS), were prepared by a simple one-pot solvothermal method. Their structures feature a wavy anionic layer of $[Sn_2S_5]_n^{2n-}$ with big windows of ten-membered rings composed of four $[SnS_4]$ and six $[SnS_5]$ polyhedra. Alkali metal cations (K^+/Rb^+) as well as H_2O molecules are located in the interlayer spaces. Both compounds show excellent removal ability for Sr^{2+} from aqueous solutions. Batch adsorption experiments show that the maximum Sr^{2+} adsorption capacities are 59.88 mg g^{-1} for FJSM-KSnS and 62.82 mg g^{-1} for FJSM-KRbSnS, respectively. FJSM-KSnS has the rapid kinetics for Sr^{2+} capture. It can reach adsorption equilibrium within 10 min with the removal rate of more than 99%. And it can maintain efficient adsorption of Sr^{2+} in a wide pH range of 4.14 to 10.05. Notably, it has good selectivity for Sr^{2+} in the presence of excessive Na^+ and even in actual environmental water samples. This work not only enriches the structural types of the thiostannate family, but also shows their great potential in the field of radiostrontium remediation.

Experimental

Materials

K_2CO_3 (AR, General-Reagent), Rb_2CO_3 (99.8%, damas-beta), S (CP, Kermel), Sn (99%, damas-beta), HNO_3 (65%–68%, China Pharmaceutical Chemical Reagents Co., Ltd), NaOH (98.00%, Greagent Reagent Co., Ltd), CsCl (99.99%, Shanghai Longjin Metal Materials Co., Ltd), NaCl (AR, Sinopharm Chemical Reagent Co., Ltd), $CaCl_2·2H_2O$ (74%, Shanghai Sili Chemical Plant), $MgCl_2$ (AR, Adamas Reagent Co., Ltd), and $SrCl_2·6H_2O$ (AR, Tianjin Guangfu Reagent Co., Ltd). All the chemicals were used without further purification.

Synthetic procedures

FJSM-KSnS and FJSM-KRbSnS were synthesized by the solvo-thermal method. A mixture of K_2CO_3 (5.0 mmol, 0.6912 g), Sn (5.0 mmol, 0.5937 g), S (15.0 mmol, 0.4808 g), and hydrazine hydrate (0.8 mL) was placed in a 28 mL stainless steel auto-clave lined with polytetrafluoroethylene (PTFE). The sealed autoclave was heated to 220 °C for 2 h and held for 3 days, which was slowly cooled down to room temperature (RT) in 12 h. The resultant solid products were isolated and then washed with water and ethanol and naturally dried to obtain pale-yellow needle-like crystals of FJSM-KSnS (yield: 0.0795 g, 6.44%, based on Sn). Additionally, K_2CO_3 (3.0 mmol, 0.4145 g), Rb_2CO_3 (2.0 mmol, 0.4620 g), Sn (5.0 mmol, 0.5937 g), S (15.0 mmol, 0.4807 g), and hydrazine hydrate (0.8 mL) were mixed. Following the same temperature control procedure and washing method as those used for FJSM-KSnS, bright-yellow needle-like FJSM-KRbSnS crystals were obtained (yield: 0.0530 g, 3.97%, based on Sn). Energy-dispersive X-ray spectroscopy (EDS) results show that the atomic ratio of the elements in FJSM-KSnS is K, 22.5%; Sn, 22.9%; and S, 54.6%. The atomic ratio of the elements in FJSM-KRbSnS is K, 12.2%; Rb, 9.5%; Sn, 23.3%; and S, 55.0%.

Characterization techniques

Single-crystal X-ray diffraction (SC-XRD) analysis was performed on a Rigaku XtaLAB Synergy-R diffractometer equipped with a graphene-monochromated microfocus MoK_α radiation source (λ = 0.71073 Å) at 100 K. Powder X-ray diffraction (PXRD) patterns were obtained using a Miniflex II diffractometer using CuK_α radiation (λ = 1.5418 Å) operated at 30 kV and 15 mA over the 2θ range of 5–65° at RT. EDS and elemental distribution mapping analysis were performed by a JEOL JSM-6700F scanning electron microscope. Thermogravimetric analysis (TGA) was performed under a nitrogen atmosphere with a NETZSCH STA449C instrument at a heating rate of 10 °C min^{-1}. Solid-state UV-vis optical diffuse reflectance spectra in the range of 800–200 nm were recorded using a Shimadzu 2600 UV-vis spectrometer at RT. X-ray photoelectron spectroscopy (XPS) analysis was performed using an ESCALAB 250Xi spectrometer with AlK_α radiation; all peaks were corrected to the C 1s peak binding energy of adventitious carbon at 284.80 eV. Inductively coupled plasma-mass spectroscopy (ICP-MS) or inductively coupled plasma-optical emission spectroscopy (ICP-OES) was used to test the concentration of ions in solution. ICP-MS and ICP-OES detection were performed using XSerise II and Thermo 7400, respectively.

Batch adsorption experiments

Typical batch adsorption experiments were carried out in 20 mL plastic bottles. 5 mg of FJSM-KSnS or FJSM-KRbSnS crystalline samples were added into 5 mL of Sr^{2+} aqueous solu-

tion (V/m = 1000 mL g^{-1}). After adsorption at RT for a period of time, the upper clarified solution was filtered through a 0.22 μm microporous membrane, diluted with 2% HNO$_3$ at different multiplicities, and then analyzed by ICP-MS or ICP-OES. Meanwhile, the samples precipitated at the bottom of the bottle were filtered and washed several times with de-ionized water and ethanol, and dried naturally for characterization, such as PXRD.

Isothermal adsorption. The solutions with Sr^{2+} concentrations from 10.39 to 1275.06 mg L^{-1} were prepared. 5 mg of FJSM-KSnS and FJSM-KRbSnS crystalline samples were added into 5 mL solution with different concentrations of Sr^{2+}, and shaken for 3 h at RT, respectively. The concentration of Sr^{2+} in the supernatant after filtration was determined by ICP-MS. Langmuir, Freundlich, and Langmuir–Freundlich models were used to fit the adsorption data and calculate the maximum adsorption capacity.

Kinetics. 20 mg of FJSM-KSnS crystalline samples were added to 20 mL of 5.32 mg L^{-1} Sr^{2+} solution and magnetically stirred at RT. About 0.3 mL of the mixture was sampled at regular intervals (2, 5, 10, 30, 60, 90, 150, 210, 300, 390, and 510 minutes), and the concentration of Sr^{2+} was determined by ICP-MS after filtration.

pH effect on adsorption. Solutions with initial Sr^{2+} concentrations of 5.36–5.51 mg L^{-1} at different acidities (pH = 2.07–12.13) were prepared by HNO$_3$ solution and NaOH solution. 5 mg of crystalline samples for FJSM-KSnS were added to 5 mL of Sr^{2+} solution with different pH values and shaken for 3 h at RT. The concentration of Sr^{2+} and the leaching rate of Sn^{4+} in the solutions were determined by ICP-MS. The solid samples were washed with water and ethanol, and the PXRD test was performed after natural drying.

Competitive ion effect. Mixed Na$^+$/Sr^{2+}, Cs$^+$/Sr^{2+}, Ca^{2+}/Sr^{2+}, and Mg^{2+}/Sr^{2+} solutions were prepared. In addition, Sr^{2+} ions were added to tap water, river water (Wulong River, Fujian, Fuzhou, China), lake water (Qishan Lake, Fujian, Fuzhou, China), and sea water (Dongshan Island, Fujian, Zhangzhou, China) to simulate contaminated actual environmental water samples. 5 mg of FJSM-KSnS crystalline samples were added to 5 mL of the above solutions and the mixtures were shaken for 3 h at RT. After filtration, the ion concentration in the solutions was determined by ICP-MS and ICP-OES.

Results and discussion

Crystal structure

Single crystal X-ray diffraction (SC-XRD) analysis confirms that both K$_2$Sn$_2$S$_5$·H$_2$O (FJSM-KSnS) and K$_{1.1}$Rb$_{0.9}$Sn$_2$S$_5$·H$_2$O (FJSM-KRbSnS) crystallize in the space group *Pbcn* and they are isostructural (Tables S1–S6). Therefore, only the structure of FJSM-KSnS as a representative is described in detail. The asymmetric unit of FJSM-KSnS contains atoms of one formula unit (Fig. S1). Sn(1) coordinates with four S atoms to form the [Sn(1)S$_4$] tetrahedron, and two [Sn(1)S$_4$] tetrahedra share the edge to form a [Sn(1)$_2$S$_6$] unit (Fig. S2a). Sn(2) coordinates with five

S atoms to form a [Sn(2)S$_5$] trigonal bipyramid. Then [Sn(2)S$_5$] trigonal bipyramids are connected together by sharing edges to generate an infinite chain along the *a*-axis (Fig. S2b). The chains are further linked by [Sn(1)$_2$S$_6$] units *via* sharing S(3) atoms resulting in a 2D wavy anionic layer of [Sn$_2$S$_5$]$_n^{2n-}$ (Fig. 1a) that contains big windows. It is found that the big window of the ten-membered ring is composed of four [SnS$_4$] and six [SnS$_5$] polyhedra in the 2D anionic layer and its size is about 13.30 × 4.36 Å^2 (Fig. 1b). The interlayer distance is 4.2449 Å (Fig. 1d and Fig. S4). K$^+$ ions and the lattice H$_2$O molecules reside in the interlayer spaces (Fig. 1c and Fig. S3). FJSM-KRbSnS has the same anionic layer as that of FJSM-KSnS, except that its interlayer spaces are filled with co-occupied K$^+$ and Rb$^+$ ions. In addition, due to the entry of Rb$^+$ into FJSM-KRBSnS, the interlayer distance in FJSM-KRbSnS slightly expands to 4.3783 Å (Fig. 1d).

At present, many thiostannates and selenostannates containing alkali metal have been reported, and they exhibit rich structural types, such as zero-dimensional 0D-Na$_4$SnS$_4$ with isolated [SnS$_4$] structural units,[44] one-dimensional 1D-K$_2$SnS$_3$·2H$_2$O containing one-dimensional thiostannate chains,[45] layered 2D-Na$_2$SnS$_3$[46] and 2D-Rb$_2$Sn$_4$Se$_9$,[47] three-dimensional microporous 3D-K$_2$Sn$_2$S$_5$[48–50] and 3D-K$_4$Sn$_4$Se$_{10}$·4.5H$_2$O.[51] Among them, 2D layered thiostannates and selenostannates are attractive due to various layered frameworks. For example, a series of 2D-*A*SnS$_2$ (*A* = Li, Na, K, and Rb) compounds have dense [SnS$_2$]$_n^{n-}$ anionic layers composed of [SnS$_6$] octahedra by sharing edges,[52] in which there is no window. In addition, although some thiostannates and selenostannates containing alkali metals have windows in the 2D anionic layer, including 2D-K$_2$Sn$_2$S$_8$,[49] 2D-Rb$_2$Sn$_4$S$_9$,[53] 2D-Na$_2$Sn$_2$Se$_5$,[54] 2D-Rb$_2$Sn$_3$S$_7$·2H$_2$O,[55] 2D-Cs$_2$Sn$_2$S$_6$,[49] 2D-Cs$_2$Sn$_3$Se$_7$,[56] 2D-Cs$_4$Sn$_5$S$_{12}$·2H$_2$O,[57] and 2D-Cs$_4$Sn$_4$Se$_{10}$·3.2H$_2$O (Fig. S5),[51] the wavy anionic layer of

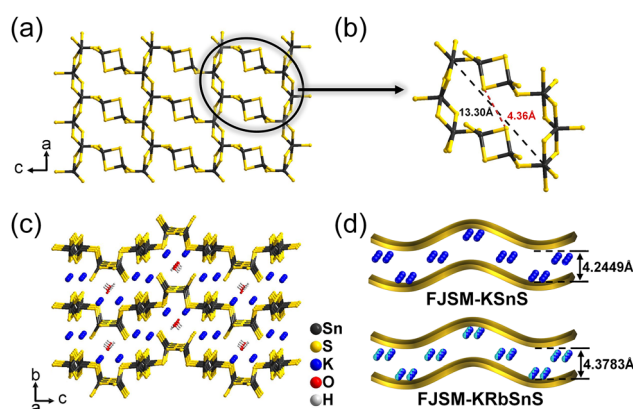**Fig. 1** (a) A 2D anionic layer of [Sn$_2$S$_5$]$_n^{2n-}$ parallel to the *ac* plane in the structure of FJSM-KSnS. (b) A big window of a ten-membered ring with the size of 13.30 × 4.36 Å^2 in the structure of FJSM-KSnS. (c) Packing of layers in FJSM-KSnS in a perspective view along the *a*-axis. (d) The schematic representation of the interlayer distances of FJSM-KSnS and FJSM-KRbSnS. The blue balls represent K atoms. The blue and green bicolored balls represent co-occupied K and Rb atoms.

$[Sn_2S_5]_n^{2n-}$ with a big window of ten-membered ring in the current thiostannates is distinct from that of these reported compounds. The anionic layers of 2D-$K_2Sn_2S_8$,[49] 2D-$Rb_2Sn_4S_9$,[53] 2D-$Na_2Sn_2Se_5$,[54] 2D-$Rb_2Sn_3S_7\cdot2H_2O$,[55] and 2D-$Cs_2Sn_2S_6$[49] contain relatively small windows. There are obviously big windows in the anionic layers of 2D-$Cs_2Sn_3Se_7$,[56] 2D-$Cs_4Sn_5S_{12}\cdot2H_2O$,[57] and 2D-$Cs_4Sn_4Se_{10}\cdot3.2H_2O$.[51] The anionic layers of 2D-$Cs_2Sn_3Se_7$[56] and 2D-$Cs_4Sn_5S_{12}\cdot2H_2O$[57] are constructed from $[Sn_3Q_{10}]$ (Q = S, Se) units with a $[Sn_3Q_4]$ semi-cubane-like core. Specifically, in the anionic layer of $Cs_2Sn_3Se_7$ twelve $[SnS_5]$ trigonal bipyramids, form a big window of a twelve-membered ring (Fig. S5g).[56] In $Cs_4Sn_5S_{12}\cdot2H_2O$ the window of ten-membered ring is formed by ten $[SnS_5]$ trigonal bipyramids (Fig. S5h).[57] $Cs_4Sn_4Se_{10}\cdot3.2H_2O$ contains $[SnSe_4]$ tetrahedra and $[SnSe_5]$ trigonal bipyramids, and the window of a ten-membered ring in its anionic layer consists of four $[SnSe_4]$ and six $[SnSe_5]$ (Fig. S5i),[51] which is similar to that of FJSM-KSnS. However, their anionic layers are still different. In $Cs_4Sn_4Se_{10}\cdot3.2H_2O$, $[Sn_2Se_6]$ units and the chain composed of $[SnSe_5]$ are connected by "trans" sharing Se(3) atoms on different sides of $[Sn_2Se_6]$ (Fig. S6a), while $[Sn_2S_6]$ units and the chain are interconnected by "cis" sharing S(3) atoms on the same side of $[Sn_2S_6]$ in FJSM-KSnS (Fig. S6b). The new connection mode leads to the formation of a new unique wavy anionic layer in FJSM-KSnS, whereas the anionic layer in $Cs_4Sn_4Se_{10}\cdot3.2H_2O$ is relatively flat (Fig. S6c and S6d). Beyond doubt, the current thiostannates are new members of the thiostannate family.

Characterization and adsorption mechanism

The PXRD patterns of FJSM-KSnS and FJSM-KRbSnS are in agreement with the simulated PXRD patterns calculated from single-crystal X-ray data (Fig. S7), indicating that pure phases of FJSM-KSnS and FJSM-KRbSnS could be synthesized by a simple one-pot solvothermal method. 50 mg of crystalline samples for FJSM-KSnS and FJSM-KRbSnS were immersed in 50 mL of 500 mg L^{-1} Sr^{2+} aqueous solutions, respectively. The mixtures were shaken for 3 h at RT, respectively. The Sr^{2+}-exchanged products (denoted as FJSM-KSnS-Sr and FJSM-KRbSnS-Sr, respectively) could be obtained after washing with water and ethanol and drying naturally. According to the PXRD results, it is confirmed that FJSM-KSnS-Sr and FJSM-KRbSnS-Sr maintain the pristine layered structure (Fig. S8). The crystal photographs confirm that FJSM-KSnS-Sr and FJSM-KRbSnS-Sr remain in their original morphology (Fig. 2a and S9). Elemental distribution maps and EDS analyses show the uniform elemental distributions and the entry of Sr^{2+} and the disappearance of some K$^+$ or Rb$^+$ (Fig. 2a, S9 and S10).

Furthermore, XPS analysis indicates that the K 2p$_{3/2}$ and K 2p$_{1/2}$ characteristic peaks of FJSM-KSnS are located at binding energies of 292.90 eV and 295.69 eV, respectively. By contrast, the characteristic peaks of K 2p in FJSM-KSnS-Sr disappear, whereas the peaks of Sr 3d$_{5/2}$ and Sr 3d$_{3/2}$ are observed at 133.74 eV and 135.45 eV (Fig. 2b–d and Table S7). Similarly, the characteristic peaks of K 2p and Rb 3d disappear in the
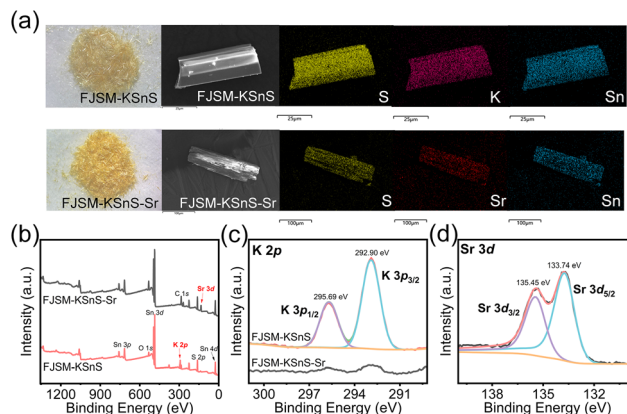

Fig. 2 (a) Photographs of crystal samples, morphologic maps, and elemental distribution mapping of FJSM-KSnS and FJSM-KSnS-Sr. (b) XPS spectra of FJSM-KSnS and FJSM-KSnS-Sr; narrow scan XPS spectra of K 2p (c) of FJSM-KSnS, and Sr 3d (d) of FJSM-KSnS-Sr.

XPS spectra of FJSM-KRbSnS, while the characteristic peaks of Sr 3d appear in those of FJSM-KRbSnS-Sr (Fig. S11 and Table S7). In summary, elemental distribution maps, EDS, and XPS results collectively demonstrate that the efficient capture of Sr^{2+} is attributed to the ion exchange between Sr^{2+} and inter-layered alkali metal ions in title thiostannates. In addition, combined with SC-XRD analysis, the compound has unobstructed and wide interlayer spaces along the a-axis direction (Fig. 1c), which allows Sr^{2+} to enter the interlayer spaces from this direction. Therefore, the ion exchange pathway likely occurs along the a-axis.

In addition, the UV-vis absorption spectra show that the optical absorption edges of FJSM-KSnS and FJSM-KRbSnS are at 490.25 nm and 473.22 nm, respectively (Fig. S12a and S12c). After Sr^{2+} adsorption, the optical absorption edges of FJSM-KSnS-Sr and FJSM-KRbSnS-Sr are red-shifted to 546.29 nm and 544.70 nm, respectively (Fig. S12b and S12d). This is consistent with the deepening of the crystal color of FJSM-KSnS and FJSM-KRbSnS compared with that of the pristine compounds (Fig. 2a and S9). TGA and DTG results showed that the weight loss percentages of FJSM-KSnS and FJSM-KRbSnS were 4.85% and 3.28%, respectively, in the range of 96–270 °C, corresponding to the loss of lattice water in FJSM-KSnS and FJSM-KRbSnS. However, it can be clearly seen that the weight loss of FJSM-KSnS-Sr and FJSM-KRbSnS-Sr increased significantly before 270 °C. This is attributed to the entering to the crystal structure of hydrated ions of Sr^{2+} ions during the ion exchange process, which carries the adsorbed H$_2$O to cause a significant increase in weight loss in TGA (Fig. S13).

Adsorption isotherm study

The maximum adsorption capacities of FJSM-KSnS and FJSM-KRbSnS at room temperature were determined through static batch experiments (Tables S8, S9 and eqn (S1)). The experimentally obtained Sr^{2+} adsorption data are fitted using

the Langmuir (eqn (S2)), Freundlich (eqn (S3)) and Langmuir–Freundlich (eqn (S4)) models. The results show that the adsorption data of both FJSM-KSnS and FJSM-KRbSnS can be well fitted with the Langmuir–Freundlich model with correlation coefficients of 0.9881 and 0.9884, respectively (Tables S10 and S11). Based on the Langmuir–Freundlich model, the maximum Sr^{2+} adsorption capacities of FJSM-KSnS and FJSM-KRbSnS are 59.88 mg g^{-1} and 62.82 mg g^{-1} (Fig. 3a and b), respectively. In addition, the maximum adsorption capacity of FJSM-KRbSnS is slightly higher than that of FJSM-KSnS. This may be due to the slightly larger interlayer spacing of FJSM-KRbSnS, and thus it is more conducive to the entry of Sr^{2+}. The adsorption capacity of FJSM-KSnS and FJSM-KRbSnS has exceeded that of some common adsorbents for Sr^{2+}, such as metal sulfides KZTS (19.3 mg g^{-1}),[40] NaZTS (32.3 mg g^{-1}),[42] metal oxysalt TaSb (26.37 mg g^{-1}),[58] KNb$_3$O$_8$ (45.6 mg g^{-1})[59] and so on. In addition, although the adsorption capacity of FJSM-KSnS is slightly lower, it is easier to synthesize. Therefore, the following adsorption experiments using FJSM-KSnS as a representative are performed.

Adsorption kinetics studies

Adsorption kinetics is an important parameter to evaluate the adsorption performance of an adsorbent. Therefore, the kinetic experiments of FJSM-KSnS capturing Sr^{2+} were carried out at room temperature (Table S12). According to the experimental results, the removal rate (R^{Sr}) of Sr^{2+} by FJSM-KSnS rapidly reaches 84.21% within 5 min (eqn (S5)). Finally, the adsorption reaches equilibrium at 10 min with a R^{Sr} value of about 99% (Fig. 3c). The pseudo-first-order (eqn (S6)) and pseudo-second-order (eqn (S7)) models are used to fit the kinetic data (Fig. S14). The latter has a high correlation coefficient (R^2 = 0.9999) (Table S13). FJSM-KSnS exhibits faster adsorption kinetics for Sr^{2+} than that of many reported adsor-

bents, such as KMS-2 (equilibrium time of 120 min)[36] and NaTS-2 (equilibrium time of 60 min).[43]

pH effect on Sr^{2+} adsorption

Generally, the pH values of the solution will affect the adsorption performance of the adsorbent. Therefore, the ability of FJSM-KSnS to adsorb Sr^{2+} in solutions with pH values of 2.07–12.13 was systematically investigated (Table S14). The experimental result shows that Sr^{2+} can be effectively removed over a wide pH range of 3.10 to 10.05 with an R^{Sr} value greater than 99% and the distribution coefficient (K_d^{Sr}) consistently greater than 10^5 mL g^{-1} (eqn (S8)). The high K_d^{Sr} value of FJSM-KSnS exceeds that reported for ZnSnS-1 (Fig. 3d).[41]

Furthermore, the leaching percentages of Sn and PXRD patterns of solid products after adsorbing Sr^{2+} in solutions with pH of 2.07–12.13 were systematically studied to confirm the stability of the current material. The leaching percentages of Sn are less than 1.1% in the pH range of 2.07 to 10.05 (Fig. S15). PXRD results confirm that the framework of FJSM-KSnS can be maintained within the pH range of 4.14 to 10.05 (Fig. S16). Therefore, FJSM-KSnS can maintain good Sr^{2+} removal ability as well as framework stability in the pH range of 4.14 to 10.05.

Competitive adsorption study

In radioactive waste liquids, a large number of competing ions usually cause a great interference to the adsorption performance of the adsorbent. Therefore, the adsorption capacity of FJSM-KSnS for Sr^{2+} in the presence of competing ions was studied (Tables S15 and S16). The experimental results show that FJSM-KSnS has excellent adsorption performance for Sr^{2+} in the presence of individual monovalent ions (e.g. Na^+). When Na/Sr molar ratios are between 14.20 and 402.65, the K_d^{Sr} values of FJSM-KSnS are consistently greater than 1.58×10^3 mL g^{-1}, and the R^{Sr} values are greater than 61.22%. Notably, when the Na/Sr molar ratio is 14.02, the separation factor ($SF_{Sr/Na}$, eqn (S9)) of FJSM-KSnS can reach a surprising value of 1943.1. Even when the Na/Sr molar ratio increases to 402.65, the $SF_{Sr/Na}$ value is still greater than 200, whereas the R^{Na} value is less than 1% (Fig. 4a). This indicates that FJSM-KSnS has high selectivity for Sr^{2+} and good separation ability for Sr^{2+} and Na^+.
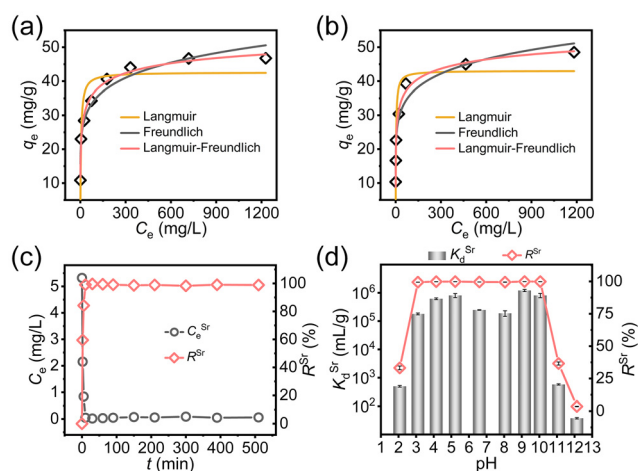

Fig. 3 Isothermal adsorption equilibrium curves of FJSM-KSnS (a) and FJSM-KRbSnS (b). (c) Kinetic curve of Sr^{2+} removal by FJSM-KSnS. (d) K_d^{Sr} and R^{Sr} values of FJSM-KSnS in solutions with different initial pH values.
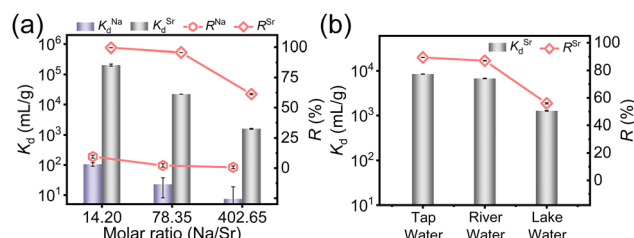

Fig. 4 (a) The K_d and R values of Sr^{2+} and Na^+ removed by FJSM-KSnS in solutions with different Na/Sr molar ratios. (b) K_d^{Sr} and R^{Sr} of FJSM-KSnS in actual water samples.

In addition, in the solution containing coexisting Cs^+ and Sr^{2+}, the selectivity of FJSM-KSnS for Sr^{2+} was explored. When the Cs/Sr molar ratio is 0.62, the K_d^{Sr} value reaches 2.43×10^5 mL g^{-1} with an R^{Sr} value of 99.59%, and the $SF_{Sr/Cs}$ value is 129.9 (Fig. S17a). The removal ability of FJSM-KSnS for Sr^{2+} gradually decreases with an increase of Cs/Sr molar ratio. When divalent ions (Ca^{2+} and Mg^{2+}) coexist with Sr^{2+}, FJSM-KSnS can remove Sr^{2+} in solutions containing lower concentrations of competing divalent ions. When the Ca/Sr molar ratio is 10.13, the K_d^{Sr} value is greater than 10^3 mL g^{-1}, and at the Mg/Sr molar ratio of 3.87, the R^{Sr} value is 88.40% (Fig. S17b and S17c).

Furthermore, low concentrations of Sr^{2+} (5.61–7.43 mg L^{-1}) were artificially added to tap water, river water (Wulong River), lake water (Qishan Lake), and sea water (Dongshan Island) to simulate polluted environmental water samples, which were used to evaluate the ability of FJSM-KSnS to capture Sr^{2+} in more complex aqueous solutions (Table S17). The results show that the R^{Sr} values of FJSM-KSnS are greater than 56% and the K_d^{Sr} values are greater than 10^3 mL g^{-1}, respectively, in simulated polluted tap water, river water, and lake water. In particular in tap water and river water, the R^{Sr} values of FJSM-KSnS can even reach 89.46% and 87.10% (Fig. 4b), respectively. In addition, the R^{Sr} value of FJSM-KSnS is 43.51% in high-salinity sea water. Therefore, FJSM-KSnS can effectively remove Sr^{2+} from actual water samples contaminated with low concentrations of Sr^{2+}.

Conclusions

In conclusion, two isomorphic alkali metal-containing thiostannates, $K_2Sn_2S_5 \cdot H_2O$ (FJSM-KSnS) and $K_{1.1}Rb_{0.9}Sn_2S_5 \cdot H_2O$ (FJSM-KRbSnS), have been synthesized by a simple one-step solvothermal method. They present wavy anionic layers with charge-balanced alkali metal cations (K^+/Rb^+) as well as H_2O molecules located in the interlayer spaces. FJSM-KSnS and FJSM-KRbSnS exhibit good Sr^{2+} capture capability with high adsorption capacity and fast kinetics. Moreover, FJSM-KSnS could maintain efficient adsorption of Sr^{2+} ($K_d^{Sr} > 10^5$ mL g^{-1}) and good framework stability over a wide pH range of 4.14 to 10.05. FJSM-KSnS has good selectivity for the removal of Sr^{2+} from actual environmental water samples. In addition, the adsorption mechanism is revealed and the efficient Sr^{2+} capture derives from ion exchange between Sr^{2+} and interlayer alkali metal ions. This study endows the thiostannate family with new members. More importantly, it further highlights the value and great potential of MSIEs, especially thiostannates, as scavengers for radionuclides.

Author contributions

Y. W. Ren: data curation, writing – reviewing and editing, validation, formal analysis, investigation, and software. J. H. Luo: structural analysis. Z. H. Chen: validation and review. S. Z. Liu: formal analysis. X. P. Guo: formal analysis. G. Y. Chen: formal analysis. M. L. Feng: conceptualization, writing – reviewing and editing, funding acquisition, resources, visualization, supervision, and project administration. X. Y. Huang: reviewing and editing, resources, visualization, and project administration.

Conflicts of interest

There are no conflicts to declare.

Data availability

Acknowledgements

References

1 E. A. Martell, *Science*, 1959, **129**, 1197–1206.

2 S. İnan, *J. Radioanal. Nucl. Chem.*, 2022, **331**, 1137–1154.

3 F. L. Zhang, J. L. Wang, Q. Q. Bi and J. Z. Du, *Sci. Total Environ.*, 2021, **764**, 144266.

4 S. P. Nielsen, *Bone*, 2004, **35**, 583–588.

5 T. L. Gerke, B. J. Little, T. P. Luxton, K. G. Scheckel and J. B. Maynard, *Environ. Sci. Technol.*, 2013, **47**, 5171–5177.

6 S. Laskar, L. Gurram, S. G. Laskar, S. Chaudhari, N. Khanna and R. Upreti, *J. Contemp. Brachytherapy*, 2015, **7**, 369–373.

7 K. Bikit, J. Knezevic, D. Mrdja, N. Todorovic, P. Kuzmanovic, S. Forkapic, J. Nikolov and I. Bikit, *Radiat. Phys. Chem.*, 2021, **179**, 109260.

8 R. C. O'Brien, R. M. Ambrosi, N. P. Bannister, S. D. Howe and H. V. Atkinson, *J. Nucl. Mater.*, 2008, **377**, 506–521.

9 J. Bruno and R. C. Ewing, *Elements*, 2006, **2**, 343–349.

10 X. Luo, G. H. Zhang, X. Wang and P. Gu, *J. Radioanal. Nucl. Chem.*, 2013, **298**, 931–939.

11 O. Kivan, M. Yusuf, R. Filson-Halliwell, J. N. Enemmoh, D. Harbottle and T. N. Hunter, *Chem. Eng. Process.*, 2025, **207**, 110077.

12 S. Kumar and R. V. S. Rao, *J. Radioanal. Nucl. Chem.*, 2021, **329**, 351–357.

13 Z. Wei, Y. Gao, Y. Zhou, C. S. Jiao, M. Zhang, H. G. Hou and W. Liu, *J. Serb. Chem. Soc.*, 2020, **85**, 909–922.

14 Q. Zhao, F. Wu, A. A. Shih, C. K. Fung, P. Y. Gao and M. X. Liu, *AlChE J.*, 2024, **70**, 1–13.

15 Y. C. Leng, J. C. Feng, Q. Jiang, Z. H. Li and H. X. Feng, *Nucl. Sci. Tech.*, 2025, **36**, 1–16.

16 L. Q. Liu, D. Y. Sun, C. Ma, S. Q. Chen, Y. F. Guo and T. L. Deng, *Chem. Eng. Sci.*, 2025, **315**, 121833.

17 Y. Park, Y. C. Lee, W. S. Shin and S. J. Choi, *Chem. Eng. J.*, 2010, **162**, 685–695.

18 X. Y. Zhang, P. Gu and Y. Liu, *Chemosphere*, 2019, **215**, 543–553.

19 P. J. Panak and A. Geist, *Chem. Rev.*, 2013, **113**, 1199–1236.

20 W. J. Paulus, S. Komarneni and R. Roy, *Nature*, 1992, **354**, 571–573.

21 Y. C. Hao, C. Hou, C. L. Chen, H. S. Zhou, Y. A. Liu, Y. Lin, H. J. Li and K. H. Hu, *Chem. – Asian J.*, 2025, **20**, 1–15.

22 Y. L. Guo, H. Y. Sun, X. Zeng, T. T. Lv, Y. X. Yao, T. H. Zhuang, M. L. Feng and X. Y. Huang, *Chem. Eng. J.*, 2023, **460**, 141697.

23 A. M. El-Kamash, *J. Hazard. Mater.*, 2008, **151**, 432–445.

24 Z. G. Ning, M. Ishiguro, L. K. Koopal, T. Sato and J. i. Kashiwagi, *J. Radioanal. Nucl. Chem.*, 2018, **317**, 409–419.

25 Y. Zhao, Y. J. Wang, X. Y. Zhang, X. L. Wang and C. Y. Qin, *New J. Chem.*, 2025, **49**, 4339–4352.

26 Q. Zheng, F. Wang, J. Y. Sun, M. F. Hamza, Q. Wu, Y. H. Z. Wu, N. C. Zheng, S. Y. Ning, T. J. Jiang, D. Q. Zeng, H. Watabe, H. Wu, Y. Wu, Y. Z. Wei and X. B. Yin, *Sep. Purif. Technol.*, 2025, **361**, 131450.

27 J. H. Tang, H. Y. Sun, W. Ma, M. L. Feng and X. Y. Huang, *Chin. J. Struct. Chem.*, 2020, **39**, 2157–2171.

28 J. H. Tang, M. L. Feng and X. Y. Huang, *Fundam. Res.*, 2024, DOI: 10.1016/j.fmre.2023.10.022.

29 J. H. Tang, S. Q. Jia, J. T. Liu, L. Yang, H. Y. Sun, M. L. Feng and X. Y. Huang, *Nat. Commun.*, 2024, **15**, 4281.

30 C. Wei, J. T. Liu, Y. Y. Zhao, S. Q. Jia, Y. J. Gao, R. A. Saha, R. Torchio, T. Zhang, L. Yang, H. Y. Sun, M. L. Feng and X. Y. Huang, *Sci. China: Chem.*, 2025, DOI: [10.1007/s11426-025-2614-x](10.1007/s11426-025-2614-x).

31 C. Lv, L. P. Liu, J. H. He, L. Yang, J. T. Liu, C. Q. Xia, X. Y. Huang and M. L. Feng, *Natl. Sci. Open*, 2024, **4**, 20240029.

32 C. Wei, S. Q. Jia, Y. Y. Zhao, J. T. Liu, H. Y. Sun, M. L. Feng and X. Y. Huang, *Separations*, 2025, **12**, 104.

33 M. J. Manos and M. G. Kanatzidis, *Chem. Sci.*, 2016, **7**, 4804–4824.

34 N. Ding and M. G. Kanatzidis, *Nat. Chem.*, 2010, **2**, 187–191.

35 M. J. Manos and M. G. Kanatzidis, *J. Am. Chem. Soc.*, 2009, **131**, 6599–6607.

36 J. L. Mertz, Z. H. Fard, C. D. Malliakas, M. J. Manos and M. G. Kanatzidis, *Chem. Mater.*, 2013, **25**, 2116–2127.

37 D. Sarma, C. D. Malliakas, K. S. Subrahmanyam, S. M. Islam and M. G. Kanatzidis, *Chem. Sci.*, 2016, **7**, 1121–1132.

38 Y. Chen, Z. X. Wang, S. R. Liu, G. H. Zhang, L. H. Dong, P. Gu and L. A. Hou, *Sep. Purif. Technol.*, 2023, **310**, 122887.

39 C. Q. Liang, M. C. Jia, X. W. Wang, Z. H. Du, J. F. Men and H. Ding, *J. Radioanal. Nucl. Chem.*, 2019, **322**, 377–387.

40 M. D. Zhang, P. Gu, Z. G. Zhang, J. Liu, L. H. Dong and G. H. Zhang, *Chem. Eng. J.*, 2018, **351**, 668–677.

41 K. Y. Wang, D. Ding, M. Sun, L. Cheng and C. Wang, *Inorg. Chem.*, 2019, **58**, 10184–10193.

42 M. D. Zhang, P. Gu, S. Yan, L. H. Dong and G. H. Zhang, *Chem. Eng. J.*, 2020, **379**, 122227.

43 J. N. Guo, Z. X. Wang, G. H. Zhang, S. R. Liu, L. H. Dong, P. Gu and L. A. Hou, *J. Radioanal. Nucl. Chem.*, 2023, **332**, 2367–2378.

44 F. Hartmann, A. Benkada, S. Indris, M. Poschmann, H. Lühmann, P. Duchstein, D. Zahn and W. Bensch, *Angew. Chem., Int. Ed.*, 2022, **61**, 1–10.

45 W. Schiwy, C. Blutau, D. Gathje and B. Krebs, *Z. Anorg. Allg. Chem.*, 1975, **412**, 1–10.

46 W. Mark, O. Lindqvist, J. C. Jumas and E. Philippo, *Acta Crystallogr., Sect. A*, 1974, **30**, 2620–2628.

47 A. K. Iyer, S. H. Ha, M. J. Waters, T. S. Ie, S. H. Shin, J. M. Rondinelli, J. I. Jang and M. G. Kanatzidis, *Chem. Mater.*, 2023, **35**, 8706–8713.

48 K. O. Klepp, *Z. Naturforsch.*, 1992, **47**, 197–200.

49 J. H. Liao, C. Varotsis and M. G. Kanatzidis, *Inorg. Chem.*, 1993, **32**, 2453–2462.

50 J. M. Yu, D. Luo, Z. J. Ma, B. Zheng, F. F. Cheng and W. W. Xiong, *ACS Appl. Mater. Interfaces*, 2021, **13**, 55188–55197.

51 A. Loose and W. S. Sheldrick, *J. Solid State Chem.*, 1999, **147**, 146–153.

52 A. Leblanc, J. Rouxel, M. Trineldu, D. Legallic and P. Perrot, *C. R. Hebd. Seances Acad. Sci.*, 1972, **274**, 786.

53 G. A. Marking, M. Evain, V. Petricek and M. G. Kanatzidis, *J. Solid State Chem.*, 1998, **141**, 17–28.

54 K. O. Klepp and M. Hainz, *Z. Anorg. Allg. Chem.*, 2000, **626**, 863–866.

55 W. S. Sheldrick and B. Schaaf, *Z. Anorg. Allg. Chem.*, 2004, **620**, 1041–1045.

56 W. S. Sheldrick and H. G. Braunbeck, *Z. Naturforsch.*, 1990, **45**, 1643–1646.

57 W. S. Sheldrick, *Z. Anorg. Allg. Chem.*, 1988, **562**, 23–30.

58 W. J. Mu, R. Zhang, X. L. Li, X. Xie, Q. H. Yu, K. Lv, H. Y. Wei and Y. Jian, *RSC Adv.*, 2015, **5**, 10378–10385.

59 J. Sun, L. Liu, X. L. Zhao, S. L. Yang, S. Komarneni and D. J. Yang, *RSC Adv.*, 2015, **5**, 75354–75359.

60 (*a*) Y.-W. Ren, J.-H. Luo, Z.-H. Chen, S.-Z. Liu, X.-P. Guo, G.-Y. Chen, M.-L. Feng and X.-Y. Huang, CCDC 2473640: Experimental Crystal Structure Determination, 2025, DOI: 10.5517/ccdc.csd.cc2p10vm; (*b*) Y.-W. Ren, J.-H. Luo, Z.-H. Chen, S.-Z. Liu, X.-P. Guo, G.-Y. Chen, M.-L. Feng and X.-Y. Huang, CCDC 2473641: Experimental Crystal Structure Determination, 2025, DOI: 10.5517/ccdc.csd.cc2p10wn.